International Journal of Nanomedicine

Dovepress
Taylor & Francis Group

Open Access Full Text Article

ORIGINAL RESEARCH

Synergistic Photothermal-Chemotherapy of Hepatocellular Carcinoma and Cancer Stem Cells via in situ pH-Responsive Hydrogels

Yunchao Wu[1,*], Xin Xu[1,*], Zhen Zhu[1], Fengyi Du[2], Guojun Zheng[1]

[1]Central Laboratory, The Affiliated Changzhou Hospital of Xuzhou Medical University, Changzhou Third People's Hospital, Changzhou, Jiangsu, 213000, People's Republic of China; [2]Jiangsu Key Laboratory of Laboratory Medicine, School of Medicine, Jiangsu University, Zhenjiang, Jiangsu, 212013, People's Republic of China

*These authors contributed equally to this work

Correspondence: Guojun Zheng, Email immu_zheng@126.com

Purpose: Monotherapy with photothermal therapy (PTT) hardly achieves durable and significant antitumor efficacy. To further improve the therapeutic effect against tumors, in this study, the chemotherapeutic agent thioridazine (THZ) was loaded into a gel network formed by the Schiff base cross-linking of amino-functionalized graphene quantum dots (NH_2-GQDs) and oxidized dextran. A pH-responsive injectable carbon dot composite hydrogel delivery system (NTD@Gel) with dual effects of photothermal therapy and chemotherapy was thereby constructed.

Methods: The techniques including HRTEM, XPS, FTIR, SEM and rheological tests were employed to verify the successful fabrication of NTD@Gel and characterize its physicochemical properties. In vitro and in vivo experiments were conducted to comprehensively evaluate the antitumor efficacy and biosafety of this hydrogel.

Results: NTD@Gel exhibited excellent photothermal conversion performance and biocompatibility, and enabled the rapid and sustained release of THZ in the acidic microenvironment. In vitro experiments confirmed that NTD@Gel could synergistically kill Hep1-6 hepatocellular carcinoma cells through photothermal ablation and THZ-induced oxidative damage, and inhibited the oncogenic Akt/Stat3 signaling pathway activation. In vivo experiments demonstrated that NTD@Gel combined with near-infrared laser irradiation significantly inhibited tumor growth, reduced CD133 and CD326 expression on tumor cells, effectively prolonged the survival time of tumor-bearing mice, and caused no obvious pathological damage in the major organs of mice.

Conclusion: NTD@Gel can significantly enhance the therapeutic efficacy against hepatocellular carcinoma and reduce the risk of metastasis and recurrence through the synergistic effect of photothermal therapy and chemotherapy.

Keywords: graphene quantum dots, thioridazine, photothermal/chemotherapy, pH-responsive hydrogel, cancer stemness

Introduction

Currently, clinical treatments for hepatocellular carcinoma (HCC) mainly include surgical resection, local ablation, transarterial chemoembolization (TACE), and systemic targeted/immunotherapy, all of which have significant limitations.[1,2] Surgery and ablation are only suitable for early-stage lesions and cannot completely eliminate multiple or invasive tumors. Although TACE realizes localized embolization chemotherapy, it may cause drug leakage, normal liver tissue injury, and procedural trauma from repeated operations.[3,4] Conventional systemic chemotherapy and targeted agents are associated with high systemic exposure and poor tumor targeting, which frequently induce adverse reactions such as myelosuppression and gastrointestinal reactions.[5] Moreover, they cannot effectively eliminate cancer stem cells or remodel the immune microenvironment,[6] leading to a high risk of recurrence and metastasis after treatment. Therefore, it is crucial to develop an efficient therapeutic platform for HCC.[7,8]

https://doi.org/10.2147/IJN.S606995
Received: 9 March 2026
Accepted: 10 May 2026
Published: 19 May 2026

Graphene quantum dots (GQDs), a type of zero-dimensional carbon-based nanomaterial derived from nanoscale-confined graphene, feature a simple and regular structure.[9] Compared with conventional nanoformulations—including liposomes (low encapsulation efficiency, rapid reticuloendothelial clearance), polymeric nanoparticles (difficulty balancing biodegradability and biotoxicity, uncertain long-term in vivo retention risks), inorganic nanoparticles (eg, gold, silica; poor degradability, potential immunogenicity), and nanoemulsions/nanocrystals (poor storage stability, large batch-to-batch variation) — GQDs exhibit more stable physicochemical properties, highly controllable preparation processes, and minimal batch differences, endowing them with great clinical translation potential.[10,11] Integrating the advantages of graphene and quantum dots, GQDs possess high photothermal conversion efficiency, good biosafety, and low preparation costs, making them promising candidates for photothermal therapy[12–14] with irreplaceable core advantages in antitumor photothermal treatment.[15,16] They have excellent near-infrared absorption capacity, enabling efficient capture of clinically applicable near-infrared laser energy and conversion of light energy into heat via non-radiative recombination and hot electron relaxation, thus showing outstanding photothermal conversion efficiency and stability.[17] Additionally, GQDs are easily surface-functionalized; through covalent or non-covalent interactions, they can load targeting molecules, chemotherapeutic drugs, fluorescent probes, and other functional components to construct multifunctional integrated diagnosis and treatment platforms. This allows synergy between tumor-targeted accumulation, fluorescence imaging, and photothermal/chemotherapy, significantly improving the precision and overall efficacy of tumor therapy.[18–21]

In recent years, with advancing research on phenothiazine antipsychotics, their potential antitumor activity has been gradually discovered.[22–24] Lu et al reported that the expression of stemness-related and cell migration-related genes in tumor cells was inhibited by THZ.[25] Zhang et al reported that the viability of cancer stem cells and sphere-forming ability could be reduced following THZ treatment.[26] Nevertheless, THZ suffers from poor water solubility and low bioavailability. Monotherapy with THZ yields limited therapeutic outcomes and various systemic adverse reactions, severely hindering its clinical translation.[27,28] Therefore, constructing an ideal delivery system to achieve targeted delivery and local sustained release of THZ is critical for enhancing treatment efficacy and reducing off-target toxicity.

Hydrogels are three-dimensional porous polymers that act as ideal platforms for drug delivery and tumor vaccination.[29,30] They allow in situ retention and sustained local release of therapeutics to prolong drug action and elevate intratumoral drug concentration.[31] With good biocompatibility and biodegradability, hydrogels minimize systemic side effects and tissue damage. Notably, hydrogels can co-load photothermal agents, chemotherapeutics and immunomodulators to realize multimodal synergistic therapy, thereby overcoming the low therapeutic efficiency of single-modal treatment.[32–35] Furthermore, injectable hydrogels function as effective carriers for tumor antigens and immune adjuvants to sustain antigen presentation, activate persistent anti-tumor immunity, and enhance immunotherapeutic outcomes.[36–38]

This study developed a novel multifunctional pH-responsive injectable hydrogel (NTD@Gel) for synergistic photothermal-chemotherapy against hepatocellular carcinoma (Scheme 1B). Fabricated via Schiff base reaction between NH_2-GQDs and oxidized dextran, this hydrogel was loaded with the chemotherapeutic agent THZ and capable of acid-responsive degradation. NH_2-GQDs were characterized for their physicochemical and photothermal properties, and oxidized dextran was successfully synthesized via sodium periodate oxidation. Subsequently, the morphology and rheological properties of NTD@Gel were systematically evaluated. In vitro experiments assessed the synergistic tumor-killing effect of NTD@Gel under near-infrared laser irradiation and THZ-induced oxidative damage in cancer cells. Further in vivo experiments investigated the long-term antitumor efficacy of NTD@Gel and its regulatory role in cancer stem cell marker expression. The pH-responsive injectable hydrogel composite constructed in this study simultaneously integrates the photothermal effect of carbon-based fluorescent nanomaterials (NH_2-GQDs), the inhibitory effect of thioridazine (THZ) on cancer stem cells (CSCs), and the acidic pH-responsive controlled-release properties of the hydrogel carrier. It achieves an integrated synergistic therapy combining drug delivery, photothermal therapy, and targeted elimination of CSCs, thereby suppressing tumor recurrence and metastasis at the source, with more comprehensive functions and superior therapeutic efficacy. This study is the first to apply the multifunctional bioagent to the combined synergistic therapy of HCC, offering novel insights and design strategies for the development of multifunctional nanocomposite hydrogels.

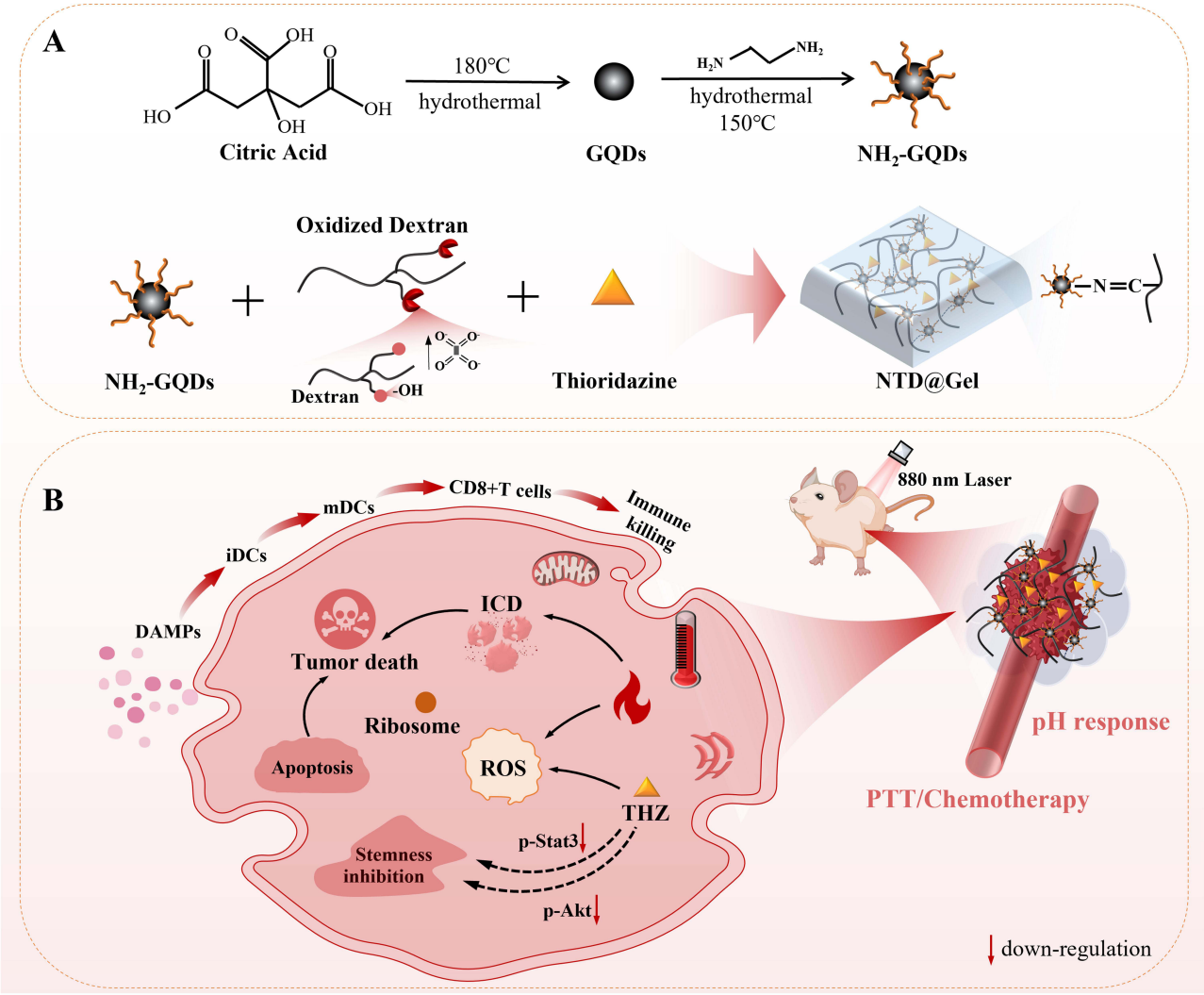

Scheme 1 (**A**) Schematic illustration of the synthesis of NTD@Gel. (**B**) In vivo antitumor mechanism and therapeutic process of the NTD@Gel.

Materials and Methods

Materials

THZ was purchased from Merck Group (Germany). 4,6-Diamino-2-phenylindole (DAPI) and CD133-PE were obtained from Thermo Fisher Scientific (USA). CD326–FITC (Ep-CAM) was purchased from BioLegend (USA). Ki67 cell proliferation assay kit, TUNEL apoptosis assay kit, cell counting kit-8 (CCK-8), reactive oxygen species (ROS) assay kit, and Calcein/PI cell viability assay kit were acquired from Beyotime Biotechnology (China). Dulbecco's Modified Eagle Medium (DMEM) and fetal bovine serum (FBS) were obtained from Hyclone (Logan, UT, USA). Anti-Phospho-Stat3 (Tyr705) and anti-Phospho-Akt antibodies were purchased from Cell Signaling Technology (USA). Anti-Nanog antibody was obtained from Abcam (UK). Dextran (MW: 40 kDa), sodium periodate, citric acid, ethylenediamine (EDA), 1,3-diphenylisobenzofuran, trypsin, and phosphate buffered saline (PBS) were acquired from Aladdin Reagent Co., Ltd. (Shanghai, China). Serum biochemical kits for blood urea nitrogen (BUN), alanine transaminase (ALT), and alkaline phosphatase (ALP) were purchased from Nanjing Jiancheng Bioengineering Institute (China). Dialysis bags with molecular weight cutoff (MWCO) of 3500 Da and 10 kDa were obtained from Biosharp Biotechnology (China). The Hep1-6 cell line was purchased from the Cell Bank of the Chinese Academy of Sciences (Cat. No. TCM39; CSTR: 19375.09.3101MOUTCM39).

https://doi.org/10.2147/IJN.S606995

Synthesis of NTD@Gel

Amino-functionalized graphene quantum dots (NH_2-GQDs) were prepared as follows: 2.0 g of citric acid powder was accurately weighed and dissolved in 50 mL of ultrapure water. The mixture was transferred into a Teflon-lined autoclave and subjected to hydrothermal treatment at 180 °C for 5 h. The resultant solution was dialyzed for 48 h using a dialysis bag (MWCO: 3500 Da) to remove unreacted small molecule impurities, yielding a graphene quantum dots (GQDs) dispersion. The as-prepared GQDs were mixed uniformly with EDA at a molar ratio of 1:5, followed by another hydrothermal reaction at 150 °C for 3 h. After further dialysis purification, the final amino-functionalized NH_2-GQDs were successfully obtained.

Oxidized dextran was synthesized via a previously reported method with minor modifications. Briefly, 10 g of dextran and 25 g of sodium periodate were dissolved in 200 mL of PBS (pH 4.5). The mixture was stirred in the dark for 1 h, and the reaction was subsequently quenched by adding 2.5 mL of diethylene glycol. The resultant solution was transferred into a dialysis bag (MWCO: 10 kDa) and dialyzed against deionized water for 3 days with daily water replacement. The purified solution was lyophilized to yield oxidized dextran.[33] The oxidation degree of the final product was determined by proton nuclear magnetic resonance (^{1}H NMR) spectroscopy, with a calculated value of 54.50%.

Preparation of NTD@Gel: 8 mg of NH_2-GQDs powder and 30 μg of THZ powder were dissolved in 1 mL of deionized water, then blended with oxidized dextran solution (160 mg/mL/240 mg/mL) at a volume ratio of 1:1. Upon rapid stirring, hydrogels formed within several seconds, which were designated as NTD@Gel_1 and NTD@Gel_2, respectively. For subsequent experiments, NTD@Gel_1 prepared at a fixed mass ratio of 1:20 was selected as the representative sample. The THZ-free composite fabricated with the same formulation was defined as ND@Gel. In addition, 8 mg of NH_2-GQDs and 15 μg of THZ were dissolved in 1 mL of deionized water, followed by the addition of 160 mg/mL oxidized dextran solution at an equal volume ratio. The resultant composite was denoted as NTD@Gel_3.

Characterization of NH_2-GQDs and NTD@Gel

The morphology and particle size distribution of NH_2-GQDs were characterized by high-resolution transmission electron microscopy (HRTEM, JEOL, JEM-2100F). Surface elemental composition of NH_2-GQDs was analyzed via X-ray photoelectron spectroscopy (XPS, Kratos, AXIS ULTRA DLD). Fourier transform infrared (FTIR) spectra were recorded using a Shimadzu IRPrestige-21. Zeta potential measurements were performed with a Zetasizer Nano ZS instrument from Malvern Instruments, UK. The ^{1}H NMR spectrum of oxidized dextran was acquired using a VARIAN VNMRS 600 spectrometer. UV-visible absorption spectra of NH_2-GQDs were determined with a Shimadzu UV3600 dual-beam ultraviolet-visible spectrophotometer. Fluorescence spectra of NH_2-GQDs were obtained using fluorescence spectrometer Edinburgh FL-FS920. Thermal images were captured by an FLIR E76 IR thermal camera (FLIR, US). The morphology of NTD@Gel was observed via scanning electron microscopy (SEM, FEI, Nova NanoSEM 450), and its rheological properties were measured using a rheometer (TA,Q800).

Photothermal Performance

Aqueous NH_2-GQDs solutions at varying concentrations (0.5, 1.0, 2.0, 3.0 and 4.0 mg/mL) were exposed to an 808 nm NIR laser at 2.0 W/cm^2, and real-time temperature variations were recorded. Meanwhile, a 3.0 mg/mL NH_2-GQDs solution was irradiated under 808 nm NIR laser with different power densities (0.25, 0.5, 1.0, 2.0 and 3.0 W/cm^2) to monitor resultant temperature changes. For photothermal stability evaluation, a 3.0 mg/mL NH_2-GQDs solution was treated with five consecutive irradiation-cooling cycles under 808 nm laser at 2.5 W/cm^2. The laser was turned off when the temperature peaked, and the solution was allowed to cool naturally to room temperature before the next cycle.[7] The photothermal conversion efficiency (η) of NH_2-GQDs was calculated according to classic reported formulas, as displayed in the subsequent content.[39]

$$\eta = \frac{hs(Tmax - Tsurr) - Q_{Dis}}{I\left(1 - 10^{-A^{\lambda}}\right)} \tag{1}$$

$$\tau s = \frac{m_D c_D}{hs} \tag{2}$$

$$\theta = \frac{\Delta T}{\Delta T_{max}} \tag{3}$$

$$t = -\tau(ln\theta) \tag{4}$$

In the above formula, h is the heat transfer coefficient, s is the surface area of the container, T_{max} represents the temperature at equilibrium, and T_{surr} represents the ambient temperature. Q_{Dis} denotes the heat dissipation of the light absorbed by the quartz cuvette, which is a constant of 37.8 mW; I is the incident laser power, and λ is the absorbance of NH_2-GQDs at 808 nm. Ts is the time constant of the sample system, and m_D and c_D are the mass and heat capacity of deionized water, respectively. θ is a dimensionless parameter. Herein, T refers to the temperature difference between the solution temperature and the ambient temperature, and T_{max} is the temperature change at the maximum steady-state temperature.

THZ Release Study

In vitro drug release experiments were performed to investigate the THZ release behavior from NTD@Gel under different pH conditions, NIR irradiation intensities, and temperatures. In brief, 2 mL of NTD@Gel complex was immersed in 20 mL of PBS buffer. The experimental conditions were set as follows: pH values of 6.5 and 7.4; NIR irradiation powers of 1.5 W, 2.0 W, and 2.5 W at pH 6.5; and temperatures of 25 °C, 35 °C, and 45 °C at pH 6.5. Aliquots of 50 μL were collected at 20-minute intervals over 100 minutes. The collected samples were then measured at 315 nm using a UV–Vis spectrophotometer to calculate the THZ release efficiency. Sink conditions were verified and maintained throughout the entire release study, with the THZ concentration in the release medium remaining below 10% of its saturation solubility at all sampling time points.

Hemolysis and Cytocompatibility Test

Fresh heparin-anticoagulated mouse whole blood was collected and rinsed three times with normal saline. The treated blood samples were incubated with NTD@Gel extracts at different dilution ratios (1:10, 1:20, 1:40 and 1:80). PBS served as the negative control, while deionized water was set as the positive control. After centrifugation at 1000 rpm for 1 min, the absorbance of each supernatant was detected via a dual-beam UV–Vis spectrophotometer to assess the hemocompatibility of NTD@Gel.[40] The hemolysis rate was calculated according to the following formula:

$$Hemolysis\ \ rate(\%) = \frac{OD_{experimentalgroup} - OD_{negativecontrol}}{OD_{positivecontrol} - OD_{negativecontrol}} \times 100\%$$

For evaluating the biocompatibility of ND@Gel, 293T cells and MEF cells were seeded into 96-well plates at a density of 1×10^4 cells per well. After cell adhesion, the cells were incubated with ND@Gel extracts at various dilution ratios (1:5, 1:10, 1:20, 1:40, 1:80). Cell viability was determined using a standard CCK-8 assay.

In vitro Cell Killing Assay

Hep1-6 cells were seeded into 96-well plates at a density of 1×10^4 cells per well. After cell adhesion, the cells were treated under different experimental conditions: PBS, NH_2-GQDs, THZ, ND@Gel, and NTD@Gel. Following 4 h of co-incubation, the cells were irradiated with an 808 nm NIR laser at 1.5 W/cm^2 for 5 min, and then incubated for an additional 1 h. Cell viability in each group was finally determined via the CCK-8 assay.

Hep1-6 cells were seeded into 24-well plates at a density of 2.5×10^4 cells per well. After cell adhesion, THZ at various concentrations (0, 500, 1000, 2000, 3000 nM) was added, and the cells were co-incubated for 24 h. Pre-diluted DCFH-DA (10 μmol/L) was then added, followed by 20 min of incubation, and fluorescence images were captured using a fluorescence microscope. A DPBF working solution (final concentration: 50 μmol/L) was prepared by diluting the DPBF stock solution with sterile PBS buffer. Cell culture supernatants from the aforementioned wells were collected and centrifuged at 4 °C and 1000 rpm for 5 min. Subsequently, 100 μL of the centrifuged supernatant was mixed with an

equal volume of DPBF working solution and gently pipetted to ensure thorough mixing. The mixture was placed in a light-shielded microplate, and the absorbance was detected at 410 nm using a microplate reader.

Hep1-6 cells were seeded into 24-well plates at a density of 2.5×10^4 cells per well. After cell adhesion, the cells were treated under different conditions (PBS, NH_2-GQDs, THZ, ND@Gel, and NTD@Gel) for 4 h. Subsequently, the cells were irradiated with an 808 nm NIR laser (power density: 1.5 W/cm^2) for 5 min, followed by an additional 12 h of incubation. After incubation, the culture medium was discarded, and the cells were gently rinsed once with pre-warmed PBS. Cells in each group were then incubated with AM-PI working solution (volume ratio: AM:PI:PBS = 1:1:1000) at 37 °C in the dark for 30 min. Following a brief rinse, fluorescence images were captured using a fluorescence microscope.

For Western blotting analysis, Hep1-6 cells from each treatment group were collected and lysed with RIPA buffer supplemented with protease inhibitors and NaF to extract total protein. The protein concentration was adjusted to 40 μg/μL, and 40 μg of protein was loaded per well. A 10% separating gel and 5% stacking gel were used for SDS-PAGE electrophoresis. Constant voltage electrophoresis was performed at 75 V for 30 min in the stacking gel, followed by 110 V for 90 min in the separating gel. Proteins were transferred onto PVDF membranes at a constant current of 300 mA for 60 min. For blocking and antibody incubation, the membranes were blocked with 5% BSA at room temperature for 1 h. Primary antibodies against p-Akt, p-Stat3 and Nanog (1:1000 dilution) were incubated overnight at 4 °C. After washing three times with TBST (5 min per wash), HRP-conjugated secondary antibodies (1:5000 dilution) were incubated for 1 h at room temperature. The membranes were washed again three times with TBST, and protein bands were visualized using an ECL chemiluminescence reagent.

For the confocal fluorescence imaging assay, Hep1-6 cells were co-cultured with NH_2-GQDs (5 μg/mL) in 24-well plates for 4 h in the dark. After three washes with PBS, the cells were labeled with DAPI. Subsequently, three organelle-specific probes (endoplasmic reticulum (ER)-Tracker Red, lysosomes (Lyso)-Tracker Red, and mitochondria (Mito)-Tracker Red) were visualized via laser scanning confocal fluorescence microscopy with an excitation wavelength of 561 nm.

Hep1-6 cells ($CD133^+CD326^+$) in the logarithmic growth phase were digested with trypsin, and the cell concentration was adjusted to 1.0×10^5 cells/mL using complete DMEM medium. The cell suspension was seeded into ultra-low attachment 96-well plates at a volume of 70 μL per well. After gentle mixing, the plates were incubated at 37 °C with 5% CO_2. Half of the medium was refreshed every three days, and cells were cultured for 7 days to observe spheroid formation.

In vivo Antitumor Study

The experimental procedures for establishing a mouse subcutaneous Hep1-6 tumor model were performed in accordance with the protocol approved by the Institutional Animal Care and Use Committee (IACUC) of Jiangsu University (Ethics Approval No: UJS-IACUC-AP-2025030505) and the Guide for the Care and Use of Laboratory Animals (Washington (DC): National Academies Press (US), 2011). Male nude mice were purchased from the Laboratory Animal Center of Jiangsu University. Male nude mice (6 weeks old) were subcutaneously inoculated with 4.0×10^6 Hep1-6 cells per mouse. When the tumor volume reached 200 mm^3, the mice were randomly divided into five groups (n = 5): (1) PBS + NIR group; (2) NH_2-GQDs + NIR group; (3) THZ group; (4) ND@Gel + NIR group; and (5) NTD@Gel + NIR group. PTT was performed using an 808 nm NIR laser at a power density of 2.0 W/cm^2 for 8 min. In vivo imaging (IVIS) was conducted at 0, 1, 3, 5, and 7 minutes post-laser irradiation to monitor photothermal effects. The corresponding formulations were intratumorally administered on days 1, 4, and 7, followed immediately by laser irradiation. Body weight and tumor volume of each mouse were measured daily. Tumor length and width were measured with a vernier caliper, and the volume was calculated using the formula: tumor volume = (tumor length × tumor width^2)/2. On day 15 after the start of treatment, all mice were euthanized via cervical dislocation following inhalation of 3% isoflurane. Blood samples, tumor tissues, and major organs (heart, liver, spleen, lungs, kidneys) were collected for subsequent experimental analysis.

The heart, liver, spleen, lung, kidney, and tumor tissues from each group of mice were fixed with paraformaldehyde, routinely embedded in paraffin, and sectioned. The sections were then stained with TUNEL, Ki-67, and hematoxylin-eosin (HE), and observed under an optical microscope. Tumor tissues were stained with mouse-derived antibodies (anti-CD133-PE and anti-CD326-FITC) and analyzed by flow cytometry. The serum concentrations of ALT, ALP, and BUN in mice from each group were determined via the colorimetric method. In vitro fluorescence imaging was performed at 1 min, 4 h, 12 h and 24 h after in situ intratumoral injection of NTD@Gel.

Statistical Analysis

All quantitative experiments were performed in triplicate or more. Data are presented as the mean ± standard deviation (SD). Statistical comparisons between two groups were performed using Student's *t*-test, and differences among multiple groups were analyzed by one-way analysis of variance (ANOVA). Statistical analyses were conducted using GraphPad Prism 10.12 software. Statistical significance was defined as $*P < 0.05$, $**P < 0.01$, $***P < 0.001$, and $****P < 0.0001$.

Results and Discussion

Preparation and Characterization of NTD@Gel

The synthesis procedure of NTD@Gel was illustrated in Scheme 1A. As shown in the HRTEM images (Figure 1A and B), NH_2-GQDs were uniform spherical nanoparticles with an average diameter of approximately 2.56 nm and a lattice spacing of about 0.22 nm. The FTIR spectrum (Figure 1C) demonstrated the presence of various functional groups on the surface of NH_2-GQDs, including hydroxyl (−OH), methylene ($-CH_2$), and amino ($-NH_2$) groups, while no amino-related chemical

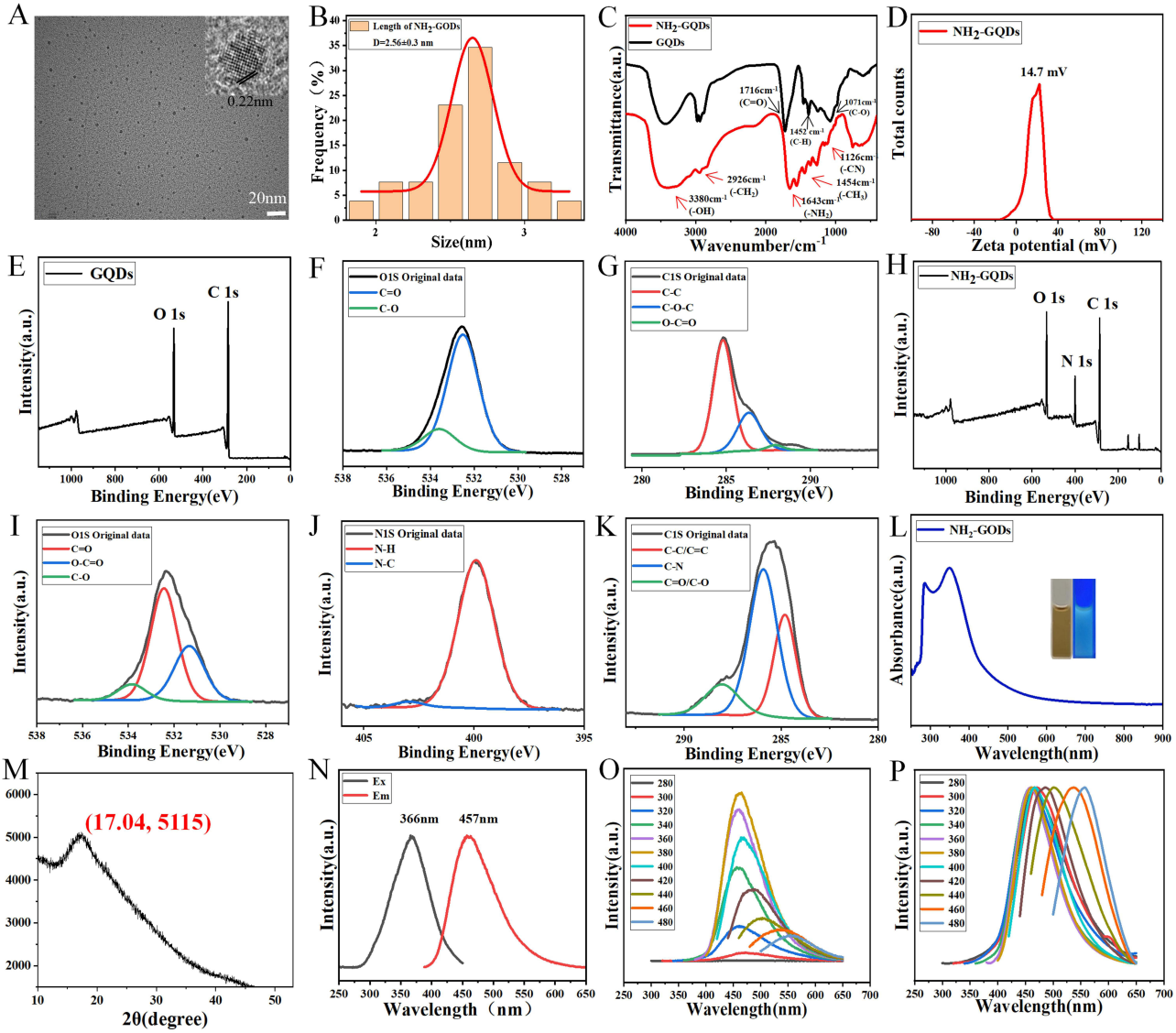

Figure 1 (**A**) Typical HRTEM images of NH_2-GQDs. (**B**) Particle size distribution of NH_2-GQDs. (**C**) FTIR spectra of GQDs and NH_2-GQDs. (**D**) Zeta potential distribution of NH_2-GQDs. (**E**) XPS survey spectra of GQDs. Peak-fitting curves for (**F**) O 1s and (**G**) C 1s. (**H**) XPS survey spectra of NH_2-GQDs. Peak-fitting spectra for (**I**) O 1s, (**J**) N 1s and (**K**) C 1s. (**L**) UV−Vis absorption spectrum of NH_2-GQDs. (**M**) XRD pattern of NH_2-GQDs. (**N**) Maximum emission spectra of NH_2-GQDs at the maximum excitation wavelength. (**O**) Photoluminescence (PL) spectra of NH_2-GQDs at different excitation wavelengths from 280 to 480 nm and (**P**) Normalized PL spectra.

https://doi.org/10.2147/IJN.S606995

bonds were detected in pristine GQDs, confirming that the surface functionalization of NH_2-GQDs was consistent with the designed objectives. These chemical groups not only provided favorable conditions for gel formation, but also endowed the material with excellent biocompatibility and water solubility. Figure 1D presented the zeta potential distribution of NH_2-GQDs. The zeta potential profile showed a single, well-defined peak centered at +14.7 mV, indicating that the amino-functionalized graphene quantum dots (NH_2-GQDs) carried a positive surface charge. This positive surface charge was attributed to the protonation of the introduced amino groups (-NH_2) on the GQD surface under aqueous conditions. This finding further verified the successful amino modification of the GQDs, which was consistent with the previous FTIR characterization results. The moderately positive zeta potential (above +10 mV) endowed the NH_2-GQDs with good colloidal stability in aqueous solution, which facilitated their uniform dispersion in the hydrogel and ensured their stable performance in subsequent biological applications.

XPS was employed to characterize the elemental composition and surface chemical states of NH_2-GQDs (Figure 1H–K). The samples consisted of three elements: C, N, and O, with characteristic peaks at 285 eV, 400 eV and 532 eV, respectively. The O 1s spectrum could be deconvoluted into three peaks assigned to C=O, C−O, and O−C=O bonds, which indicated that the surface of NH_2-GQDs retained abundant active sites for the amination. Notably, the N 1s spectrum was fitted into two major peaks corresponding to N−H and N−C bonds. These results directly confirmed the existence of free amino groups (−NH_2) on NH_2-GQDs, which supplied crucial active sites for the subsequent Schiff base cross-linking reaction with oxidized dextran. Meanwhile, Figure 1E–G showed that pristine GQDs contained only C and O elements. This comparison further validated the successful amino functionalization of NH_2-GQDs. As shown in Figure 1L, the aqueous NH_2-GQDs solution appeared brownish-yellow and transparent under natural light, and emitted blue-green fluorescence under UV irradiation. In UV–Vis absorption spectrum, a distinct maximum absorption peak was observed at 350 nm, with its absorption tail extending into the visible region, which confirmed the excellent fluorescence properties of NH_2-GQDs. The X-ray diffraction pattern of NH_2-GQDs (Figure 1M) displayed a broad diffraction peak at 17.04^0, revealing the amorphous structure of NH_2-GQDs. The fluorescence spectrum of NH_2-GQDs (Figure 1N) showed the maximum excitation peak at 366 nm, which represented the optimal excitation wavelength for producing QD fluorescence. The strongest emission peak appeared at 457 nm, consistent with the characteristic blue-green fluorescence. This emission fell in the short-wavelength visible region, endowing NH_2-GQDs with good tissue penetration and low background fluorescence interference. Figure 1O and P presented the original and normalized fluorescence emission spectra of NH_2-GQDs under excitation wavelengths ranging from 280 to 480 nm, respectively. As the excitation wavelength increased, the fluorescence intensity first rose and then declined, peaking at 380 nm. Spectral normalization eliminated intensity discrepancies and clearly illustrated the changes in emission peak position and profile with excitation wavelength. The emission peak gradually red-shifted from 460 nm to 560 nm, and longer excitation wavelengths slightly broadened the full width at half maximum (FWHM) of the emission peaks.

To verify the successful oxidation of dextran and calculate the oxidation degree, ^{1}H NMR analysis was performed on the samples (Figure 2A). By comparing the signal at 4.88 ppm between the aldehyde-functionalized and non-aldehyde-functionalized repeating units and integrating the corresponding peaks, the oxidation degree of the oxidized dextran was calculated to be 54.50%. As shown in Figure 2B, the digital photograph of NTD@Gel displayed a brown and opaque gel. The sample exhibited no flow upon centrifugal tube inversion, confirming successful gel formation. FTIR spectroscopy was used to investigate the chemical bonds of NTD@Gel and ND@Gel (Figure 2C). In NTD@Gel_1 and NTD@Gel_2, a medium-strong peak at 1605 cm^{-1}, assigned to the stretching vibration of Schiff base linkages (−C=N−), verified the occurrence of Schiff base cross-linking between the aldehyde groups (−CHO) of oxidized dextran and amino groups (−NH_2) of NH_2-GQDs, forming stable covalent −C=N− bonds. Notably, no characteristic absorption of aldehyde groups (−CHO) was detected at approximately 1720 cm^{-1}, which further evidenced the extensive involvement of aldehyde groups in the cross-linking process. Strong absorption peaks were observed at 1145 cm^{-1} and 1009 cm^{-1}, corresponding to the stretching vibrations of the glycosidic bond C−O−C and the cyclic C−O bond of the sugar unit, respectively. This indicated that the polysaccharide backbone of dextran remained intact during the cross-linking reaction and maintained its structural integrity. In comparison, ND@Gel_1 showed no absorption peaks corresponding to the characteristic functional groups of THZ (C≡N bond at 1605 cm^{-1}). These results elucidated the cross-linking mechanism between NH_2-GQDs and oxidized dextran, confirming both the formation of Schiff base linkages and the successful construction of the NTD@Gel network architecture. SEM images of lyophilized NTD@Gel_1 and NTD@Gel_2 (Figure 2D) revealed

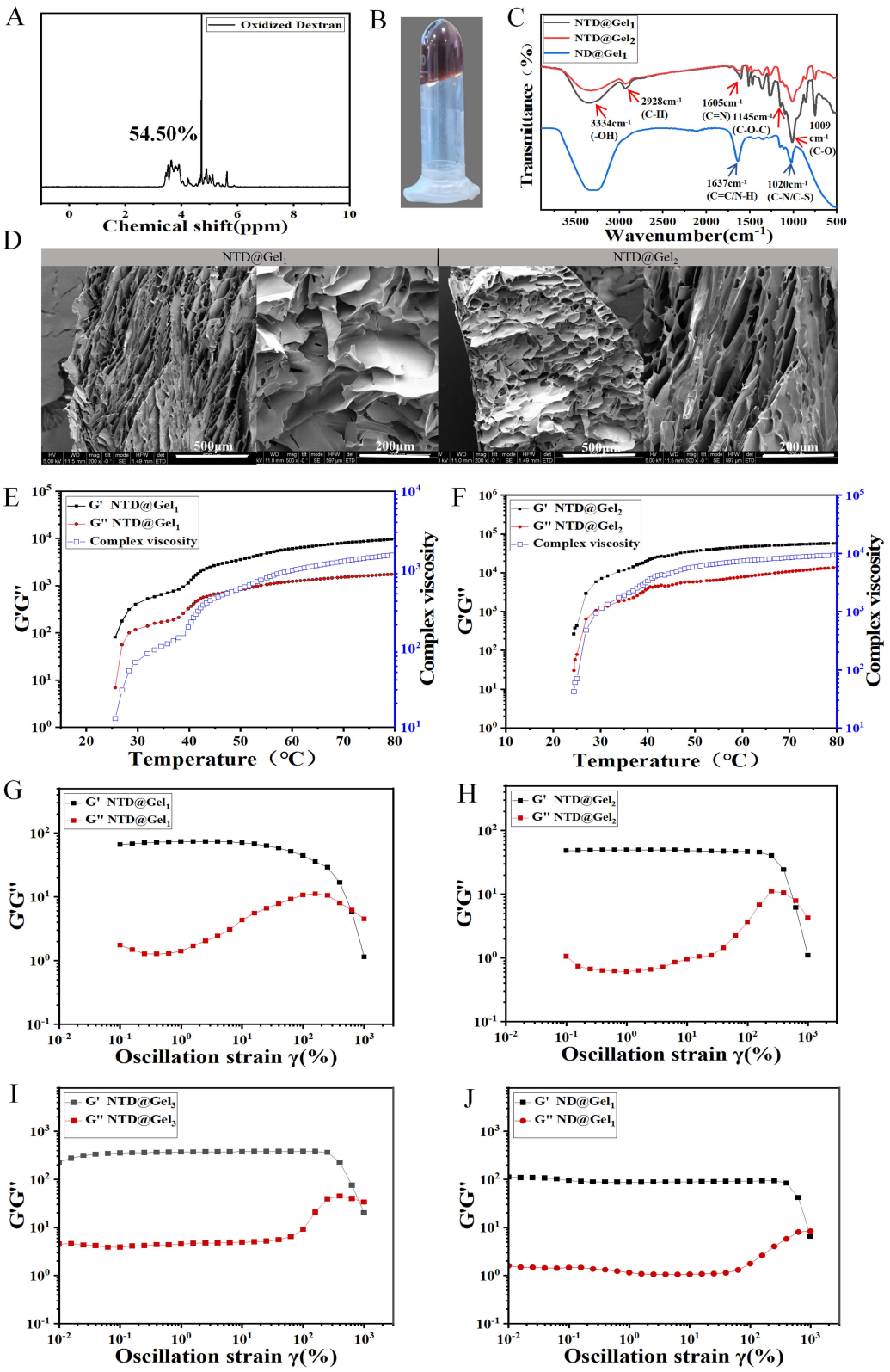

Figure 2 (**A**) ^{1}H NMR spectrum of oxidized dextran. (**B**) Digital photograph of NTD@Gel. (**C**) FTIR spectra of NTD@Gel$_1$, NTD@Gel$_2$ and ND@Gel$_1$. (**D**) SEM images of NTD@Gel$_1$ and NTD@Gel$_2$. Temperature-dependent rheological curves of (**E**) NTD@Gel$_1$ and (**F**) NTD@Gel$_2$. Strain amplitude sweep tests (37 °C, 1 Hz) of (**G**) NTD@Gel$_1$, (**H**) NTD@Gel$_2$, (**I**) NTD@Gel$_3$ and (**J**) ND@Gel$_1$.

https://doi.org/10.2147/IJN.S606995

that both hydrogels exhibited a uniform, interconnected porous network structure, and the pore size showed no obvious correlation with the gelation ratio. This typical scaffold structure was crucial for the stability, biological properties, and sustained drug release capacity of the hydrogels. Temperature-dependent rheological curves of NTD@Gel_1 and NTD@Gel_2 are shown in Figure 2E and F. At room temperature (25 °C), the storage modulus (G′), loss modulus (G ″), and complex viscosity of NTD@Gel remained relatively low. These parameters gradually increased with rising temperature and tended to stabilize above 50 °C. These results demonstrated that the NTD@Gel system could maintain a stable elastic scaffold structure under variable temperature conditions. Oscillatory strain-dependent rheological curves of NTD@Gel_1, NTD@Gel_2, NTD@Gel_3 and ND@Gel_1 are presented in Figure 2G–J. In the low oscillatory strain region, G′ > G″, and the hydrogel maintained a relatively stable structure. With increasing oscillatory strain, G′ gradually decreased, while G″ first increased and then decreased. Eventually, the two moduli intersected (629% in Figure 2G, 628% in Figure 2H, 825% in Figure 2I and 919% in Figure 2J), corresponding to the collapse of the elastic network. These rheological behaviors endowed NTD@Gel with suitable mechanical performance for in situ injection. Different feeding ratios of oxidized dextran exerted little influence on gel mechanical properties. By comparison, the introduction of THZ slightly impaired the strain resistance of the hydrogel, and higher THZ content aggravated this weakening effect.

Photothermal Property of NH_2-GQDs

The photothermal conversion capability of NH_2-GQDs was further investigated. Aqueous NH_2-GQDs solutions of different concentrations were irradiated with an 808 nm laser at a power density of 2.0 W/cm^2 (Figure 3A). The solution temperature rose gradually with irradiation time and plateaued at 10 min, with a maximum temperature of 52.1 °C. As shown in Figure 3B, NH_2-GQDs solution (3.0 mg/mL) was irradiated by an 808 nm laser at different power densities. The temperature increased with irradiation duration and stabilized at 10 min. The maximum temperature exhibited a positive correlation with laser power density; notably, the temperature reached 64.7 °C at 3.0 W/cm^2. As illustrated in Figure 3C and D, the temperature of the NH_2-GQDs solution remained stable during five consecutive on-off laser irradiation cycles, demonstrating that NH_2-GQDs possessed stable and repeatable photothermal conversion performance. Based on the cooling curve, the photothermal conversion efficiency of NH_2-GQDs was calculated to be 21.8%. Figure 3E and F showed the corresponding photothermal images, respectively. Figure 3G showed the photothermal infrared image of NTD@Gel. Upon irradiation at a power intensity of 2.5 W/cm^2 for 9 minutes, the temperature reached 58.3 °C, indicating that NH_2-GQDs still maintained an effective photothermal effect after forming a gel via Schiff base reaction, which provided a reliable experimental basis for subsequent in vivo studies.

pH-Responsiveness and Biocompatibility of NTD@Gel

To investigate the release behavior and influencing factors of THZ from NTD@Gel, we conducted in vitro simulated THZ release experiments under different pH conditions, different irradiation intensities, and different temperatures. Figure 4A showed that THZ was rapidly released within 0–40 min at pH 6.5. The cumulative release rate reached 38.6% at 20 min and 66.4% at 40 min. The release slowed markedly after 40 min, with the cumulative release approaching 73.4% at 100 min. By comparison, NTD@Gel exhibited an extremely low drug release level throughout the test at pH 7.4, maintaining a steady release ratio of only 8.0%. These results verified the pH-responsive drug release performance of the NTD@Gel hydrogel. Fitted by the Korsmeyer-Peppas model, drug released at pH 6.5 was primarily dominated by diffusion, accompanied by a moderate auxiliary process of pH-responsive swelling. As shown in Figure 4B and C, the release profiles of THZ from NTD@Gel exhibited no significant differences under different irradiation intensities (1.5–2.5 W) and temperatures (25–45 °C). The cumulative release rates of all groups were approximately 75% at 100 min, indicating that irradiation intensity and temperature had no significant effect on the drug release behavior of this system. The blood compatibility of NTD@Gel hydrogels was further evaluated via a red blood cell hemolysis assay. As shown in Figure 4D, the hemolysis rates of samples after co-incubation at different ratios were all far below the 5% safety threshold for biomaterials. Even at the highest extract concentration (1:10), the hemolysis rate was only 2%, with no significant differences among the groups. The CCK-8 assay was used to evaluate the cytocompatibility of ND@Gel (Figure 4E and F). After 293T and MEF cells were cultured with ND@Gel extracts at various dilutions, the cell viability remained above 95%, indicating the excellent biocompatibility of ND@Gel.

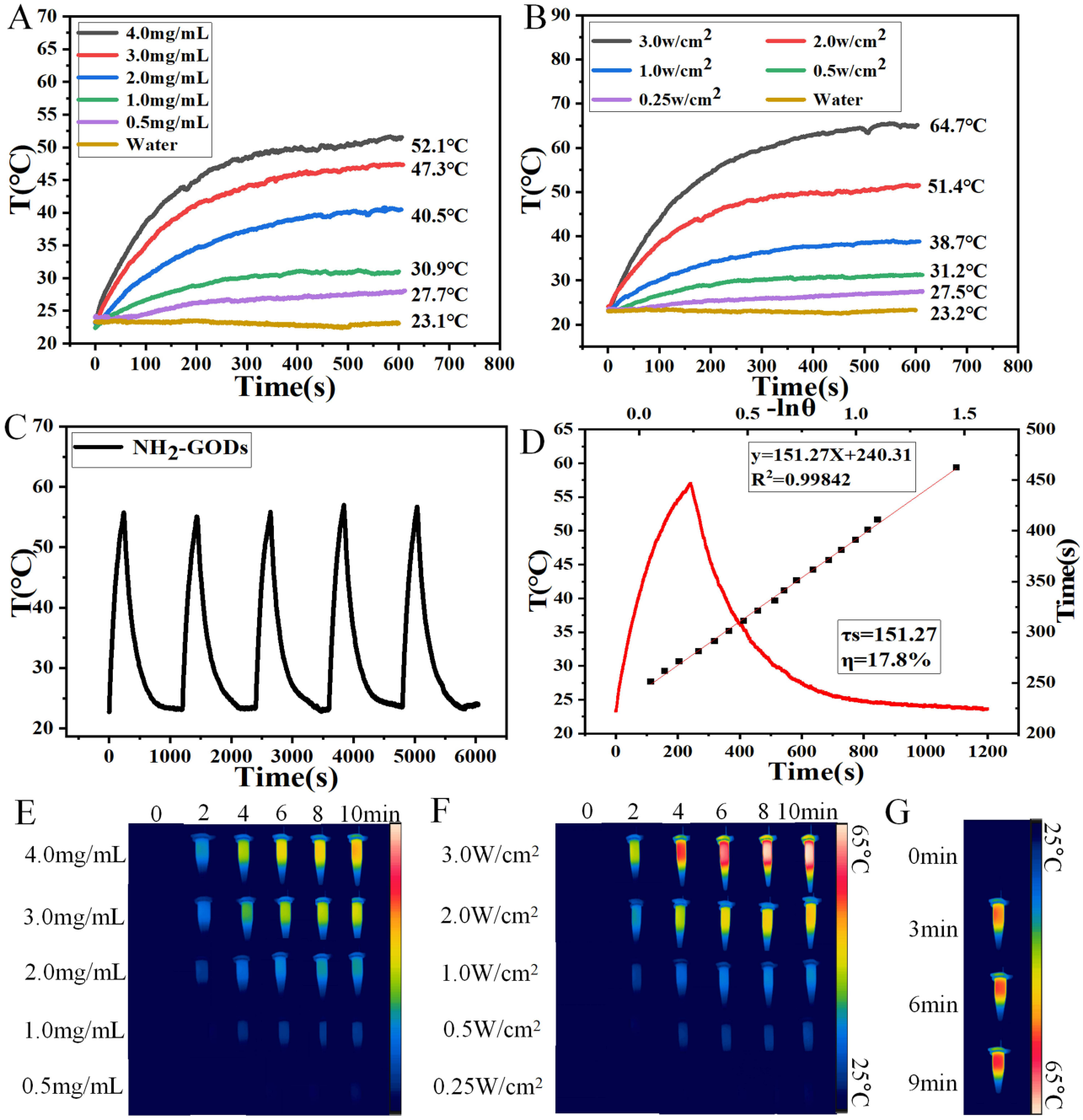

Figure 3 (**A**) Temperature curves of NH_2-GQDs solutions with different concentrations (0.5–4.0 mg/mL) under 808 nm NIR irradiation at a power density of 2.0 W/cm^2. (**B**) Temperature curves of NH_2-GQDs solution (3.0 mg/mL) under 808 nm NIR irradiation at different power densities (0–2.5 W/cm^2). (**C**) Heating curves of the NH_2-GQDs solution for five laser on/off cycles under irradiation with an 808 nm NIR laser (2.5 W/cm^2). (**D**) Temperature curve of NH_2-GQDs solution after 240 s NIR laser (808 nm, 2.5 W/cm^2) irradiation and cooling; linear time data vs -ln θ was obtained from the cooling stage. (**E** and **F**) Corresponding infrared thermal images. (**G**) Photothermal imaging of NTD@Gel (2.5 W/cm^2).

In vitro Cytotoxicity Assay of THZ and NTD@Gel

CCK-8 assay was adopted to evaluate the cell viability of each treatment group (Figure 5A). Compared with the NH_2-GQDs+NIR and THZ groups, ND@Gel and NTD@Gel exhibited remarkable cell killing ability. NTD@Gel exerted the strongest cytotoxic effect, suggesting its great prospect in antitumor therapy.

ROS generation was detected to evaluate THZ-induced oxidative stress (Figure 5B and E). Intracellular ROS was labeled with green DCF fluorescence, and cell nuclei were stained blue with DAPI. After Hep1-6 cells were treated with

https://doi.org/10.2147/IJN.S606995

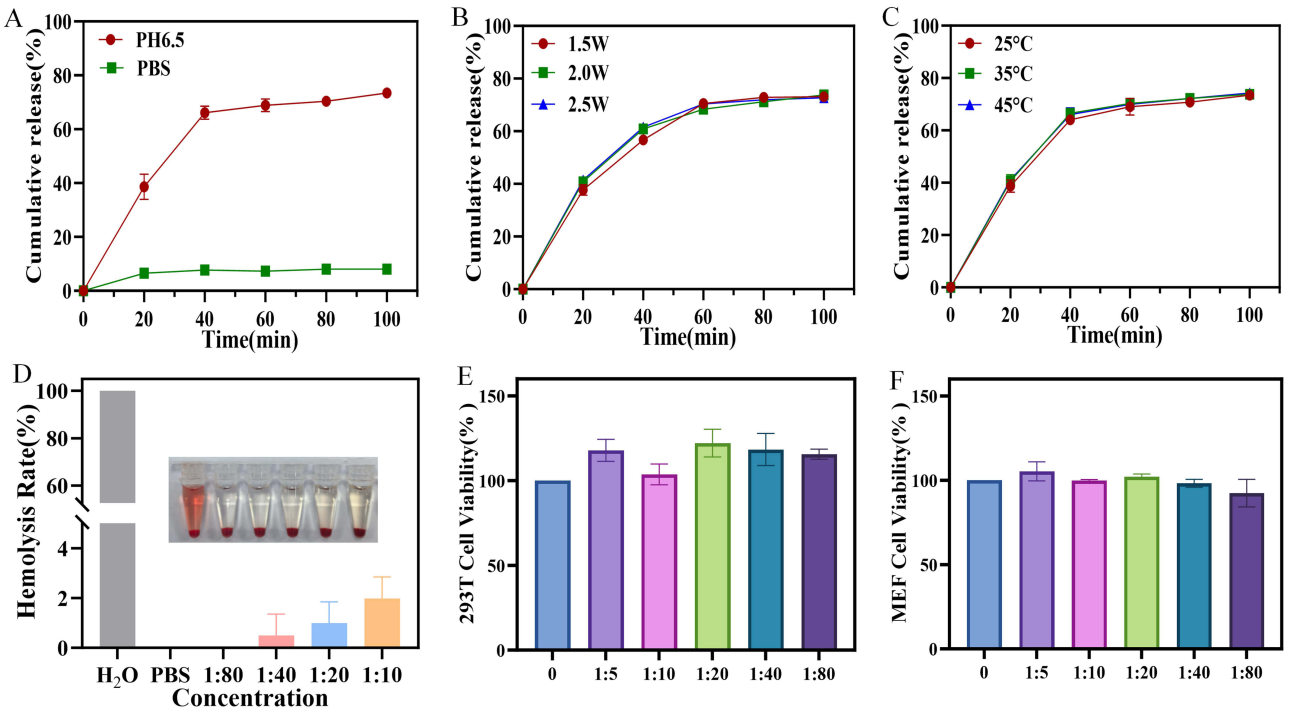

Figure 4 Accumulated release profiles of THZ from NTD@Gel under (**A**) different pH conditions, (**B**) different near-infrared irradiation intensities (1.5, 2.0, and 2.5 W) and (**C**) different temperatures (25, 35, and 45 °C) (n = 3). (**D**) Hemolysis images and hemolysis rate of red blood cells co-incubated with NTD@Gel hydrogel extracts at different dilution ratios (1:10, 1:20, 1:40, 1:80) (n = 3). (**E** and **F**) Cytocompatibility of ND@Gel of different concentrations (n = 3).

gradient concentrations of THZ (0, 500, 1000, 2000, 3000 nM, left to right), intracellular ROS levels increased in a concentration-dependent manner. Higher THZ concentration triggered greater ROS accumulation, which induced oxidative stress damage. This trend revealed that the antitumor effect of THZ was closely correlated with ROS-mediated oxidative stress.

A live/dead cell staining assay was employed to directly evaluate the killing effect of different treatments on Hep1-6 cells (Figure 5C and F). The cell death rates in the ND@Gel+NIR and NTD@Gel+NIR groups were significantly higher than those in the NH_2-GQDs+NIR and THZ groups, with the NTD@Gel+NIR group exhibiting the highest cell death rate. This result intuitively demonstrated that the combination of THZ-induced cytotoxicity and the direct killing effect of PTT could significantly enhance the killing efficacy against Hep1-6 cells.

A Western blot (WB) assay was used to investigate the tumor suppressor-related signaling pathways involved in THZ (Figure 5D). Compared with the other three groups, the protein expression levels of p-Akt, p-Stat3 and Nanog were all downregulated in the THZ group and the NTD@Gel+NIR group. These results indicated that THZ inhibited the activation of oncogenic signaling pathways by downregulating the protein expression of p-Akt, p-Stat3 and Nanog. Meanwhile, combined treatment with NTD@Gel plus NIR irradiation also effectively blocked the activation of this pathway. The above findings confirmed that the Akt/Stat3 signaling pathway acts as a key therapeutic target for hepatocellular carcinoma treatment using NTD@Gel combined with NIR therapy, providing experimental evidence for the antitumor mechanism of this synergistic system.

To evaluate the extracellular singlet oxygen ($^1O_2$) concentration in different treatment groups, the DPBF probe assay was performed. As shown in Figure 5G, the characteristic absorption peak of DPBF exhibited significant differences among groups after various treatments. THZ showed a certain ability to induce $^1O_2$ generation; the absorbance of the ND@Gel+NIR and NTD@Gel+NIR groups was further decreased, demonstrating that the combined system possessed the strongest $^1O_2$ generation capacity under NIR irradiation, which could induce more severe cellular oxidative stress. This result was consistent with the intracellular ROS detection results, providing direct evidence at the cellular level for its ability to induce oxidative damage in tumor cells.

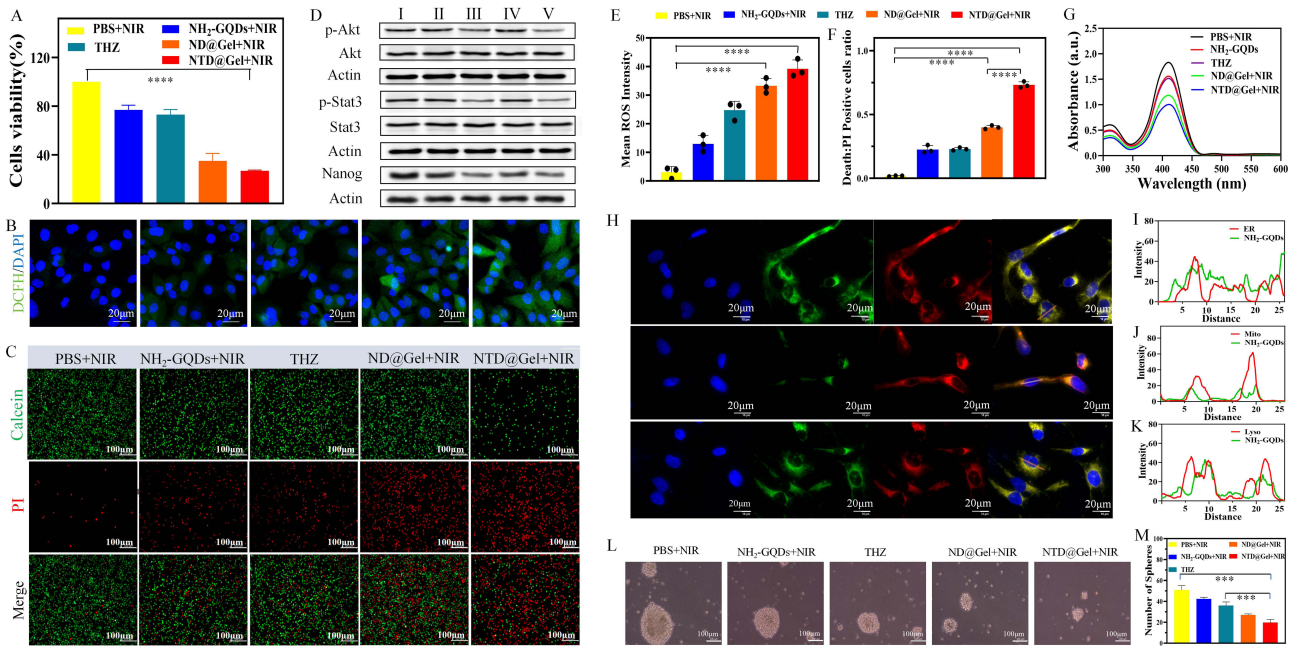

Figure 5 (**A**) Cell viability of Hep1-6 cells after various treatments detected by CCK-8 assay (n = 3). (**B**) Confocal fluorescence images of intracellular ROS levels in Hep1-6 cells treated with different concentrations of THZ. Scale bar: 10 μm. (**C**) Laser confocal images of live/dead staining under different treatments. Scale bar: 100 μm. (**D**) Protein expression levels of p-Akt, p-Stat3 and Nanog in each group. (**E** and **F**) Corresponding quantitative analysis (n = 3). (**G**) Singlet oxygen ($^1O_2$) production capacity of different treatment groups. (**H**) Fluorescence colocalization images of specific organelle probes (red) and NH_2-GQDs (green) in Hep1-6 cells; (**I**–**K**) Corresponding linear profile analysis. (**L**–**M**) Inhibition of tumor sphere formation by NTD@Gel-mediated synergistic therapy.*P < 0.05, **P < 0.01, ***P < 0.001, ****P < 0.0001.

To clarify the intracellular distribution and subcellular localization characteristics of NH_2-GQDs, we performed immunofluorescence colocalization assays to investigate the colocalization of NH_2-GQDs with the ER, Mito and Lyso, respectively. Linear intensity analysis was further applied to verify the degree of colocalization. As shown in Figure 5H–K, after 4 h of co-incubation, fluorescence signals of NH_2-GQDs were detected to varying degrees in the ER, Mito, and Lyso of Hep1-6 cells. These results suggested that upon entering cells, NH_2-GQDs were primarily internalized via the endocytic pathway and subsequently transported to and enriched in Lyso, with only a small fraction distributed in the ER and Mito. This indicated that Lyso served as the main intracellular metabolic site for NH_2-GQDs, while the risk of direct toxicity to the ER and Mito is low, with limited potential impacts on these organelles.

The results of the tumor sphere formation assay (Figure 5L and M) showed that the NTD@Gel+NIR treatment group exhibited the fewest and smallest tumor spheres, significantly outperforming all control groups including PBS+NIR, NH_2-GQDs+NIR, THZ, and ND@Gel+NIR. Quantitative analysis confirmed that NTD@Gel-mediated photothermal-chemotherapy synergistic treatment significantly inhibited the self-renewal capacity of liver cancer stem cells, with an effect markedly superior to that of monotherapy modalities. These results indicated that this dual-responsive system can effectively attenuate tumor stemness, holding promise for reducing the risk of tumor recurrence after treatment.

In vivo Antitumor Effect of NTD@Gel

Based on the excellent photothermal effect and tumor cell killing ability of NTD@Gel, in vivo validation experiments were further designed in tumor-bearing mice (Figure 6A). Figure 6B shows the photographs of the excised tumors after different treatments. To clarify the local temperature of the hydrogel at the tumor site, we performed in vivo thermal imaging of the mice using a thermal imager. As shown in Figure 6C, the PBS and NTD@Gel groups were irradiated separately. At 0 min, no obvious thermal effect was observed in either group. With the extension of irradiation time, the temperature at the injection site of NTD@Gel gradually increased and stabilized at 47 °C at 7 min, while only a slight temperature elevation was detected in the PBS group. These results directly confirmed the ability of NTD@Gel to form an in situ thermal island at the injection site. Such localized heating effectively induces tumor cell apoptosis, providing the essential thermal condition for synergistic photothermal-chemotherapy. The body weight of mice in each group was

https://doi.org/10.2147/IJN.S606995

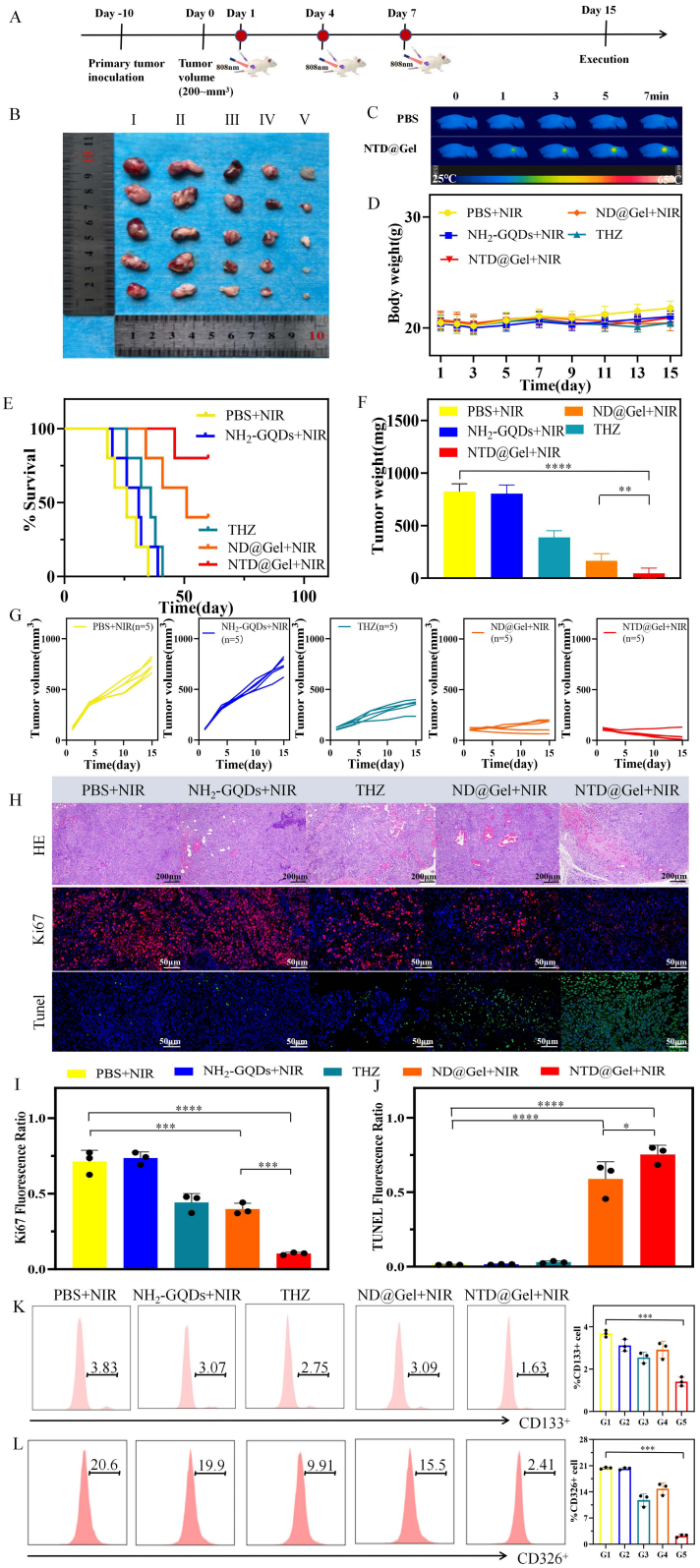

Figure 6 In vivo photothermal effect of NTD@Gel and its inhibitory effect on tumor growth. (**A**) Schematic of the experimental design. (**B**) Tumor images after different treatments. (**C**) In situ infrared thermal images of tumors in NTD@Gel and control (PBS) groups during 808 nm laser irradiation (2.0 W/cm^2) for 7 min. (**D**) Body weight change curves, (**E**) survival curves, (**F**) average tumor weight, and (**G**) tumor volume change curves of mice in different treatment groups over 15 days (n = 5). (**H**) H&E-stained (Scale bar: 200 μm), Ki67 and TUNEL (Scale bar: 50 μm) fluorescence staining images of tumor tissue sections from different treatment groups. (**I** and **J**) Corresponding quantitative analyses (n = 3). Flow cytometric analysis of (**K**) CD133 and (**L**) CD326 expression in tumor tissue cells from different treatment groups. *P < 0.05, **P < 0.01, ***P < 0.001, ****P < 0.0001.

https://doi.org/10.2147/IJN.S606995

plotted as a line graph (Figure 6D). The body weight of all groups remained relatively stable, and no systemic weight loss was observed over the entire experimental period. Figure 6E shows the survival curves of each group. The 30-day survival rates of the PBS+NIR, NH_2-GQDs+NIR, and THZ groups were relatively low, with all mice dead within 38 days. Although the THZ monotherapy group prolonged survival to a certain extent, the effect was limited. The survival rate of the ND@Gel+NIR group was 50% at day 60. The NTD@Gel+NIR group exhibited the highest survival rate of 80% at day 60, indicating the most significant survival benefit. These results confirmed that the in situ photothermal-immunomodulatory hydrogel possessed excellent antitumor efficacy and could significantly prolong the survival time of tumor-bearing mice. Figure 6F showed that the NTD@Gel+NIR group had the lowest tumor weight, significantly lower than all other groups, indicating the strongest anti-tumor effect of this synergistic therapy. The in vivo anti-tumor results showed that the tumor volumes in both the ND@Gel+NIR and NTD@Gel+NIR groups were significantly smaller than those in the PBS+NIR, NH_2-GQDs+NIR, and THZ monotherapy groups (Figure 6G). Among them, the NTD@Gel+NIR synergistic treatment group exhibited the smallest tumor volume, with a corresponding tumor growth inhibition rate as high as 94.17%, which was significantly superior to the NH_2-GQDs group (1.04%), THZ monotherapy group (53.61%), and ND@Gel+NIR group (80.03%). These results confirmed that NTD@Gel-mediated combined photothermal-chemotherapy exerted a strong synergistic anti-tumor effect, with efficacy far superior to single treatment modalities.

The effects of different treatments on tumor tissues were systematically evaluated from three dimensions: tissue morphology, cell proliferation activity, and apoptosis level (Figure 6H–J). HE staining showed varying degrees of histiocytic necrosis in all groups except the PBS+NIR group, with the most severe damage observed in the NTD@Gel +NIR group. Ki67 and TUNEL immunofluorescence staining clearly revealed that tumor cells in the PBS+NIR group proliferated vigorously with only mild apoptosis. In contrast, the NTD@Gel+NIR group showed significant inhibition of tumor cell proliferation and a large number of apoptotic cells. These three sets of results were highly consistent, collectively confirming that NTD@Gel-mediated synergistic photothermal-chemotherapy could effectively kill tumor tissues through multi-mechanism synergy. Its therapeutic effect was significantly superior to single photothermal therapy, single chemotherapy, or drug-free hydrogel-mediated photothermal therapy.

Flow cytometry was used to detect the expression of cancer stem cell markers (CD133 and CD326) in tumor tissues of different treatment groups (Figure 6K and L). The PBS+NIR group had the highest CD133-positive proportion (3.83%), while the NTD@Gel+NIR group showed the lowest (1.63%), with a significant reduction (***$P < 0.001$); other groups had slight decreases (3.07–3.09%). For CD326, the PBS+NIR group had the highest positive proportion (20.6%); the NTD@Gel+NIR group exhibited the most significant reduction to 2.41% (***$P < 0.001$), while other groups had moderate to slight decreases (9.91–19.9%). As core stemness markers of hepatocellular carcinoma, CD133 and CD326 are associated with tumor recurrence and metastasis. NTD@Gel+NIR treatment significantly downregulated both markers, indicating that this synergistic therapy can not only eradicate tumor cells but also reduce tumor recurrence and metastasis risk.

Major organs (heart, liver, spleen, lung and kidney) of experimental mice were collected for H&E staining and histological pathological analysis. As shown in Figure 7A, the tissue structure and cell morphology of all major organs remained intact in each group. Semi-quantitative histological scoring (0–3 scale) for inflammatory infiltration, degeneration/necrosis, edema/congestion and fibrosis revealed scores ≤ 1 in all groups, with no significant difference relative to the PBS+NIR control. Figure 7B–D showed the renal and hepatic function markers of mice in different treatment groups. Serum levels of urea nitrogen (BUN), alanine aminotransferase (ALT), and alkaline phosphatase (ALP) were all within the normal physiological range and showed no intergroup differences. These results indicated that NTD@Gel and other treatments induced no obvious hepatorenal toxicity. Collectively, NTD@Gel displayed favorable in vivo biocompatibility.

This ex vivo fluorescence imaging (Figure 7E) result showed that after intratumoral injection of NTD@Gel, strong fluorescence signals of NH_2-GQDs were concentrated at the tumor site at 1 min and 4 h post-injection, with only weak transient signals observed in the heart, liver, spleen, and kidney at 4 h. By 12 h, only faint fluorescence remained in the tumor, with no obvious residual signals in the organs, and almost no fluorescence was detected in tumors or major organs at 24 h. These findings demonstrated the excellent tumor localization capability of NTD@Gel, which prolonged NH_2-GQDs retention at tumor sites, restricted systemic diffusion, and reduced exposure and potential toxicity to normal tissues. The time-dependent attenuation of fluorescence, together with transient organ signals at 4 h and complete clearance within 24 h,

 https://doi.org/10.2147/IJN.S606995

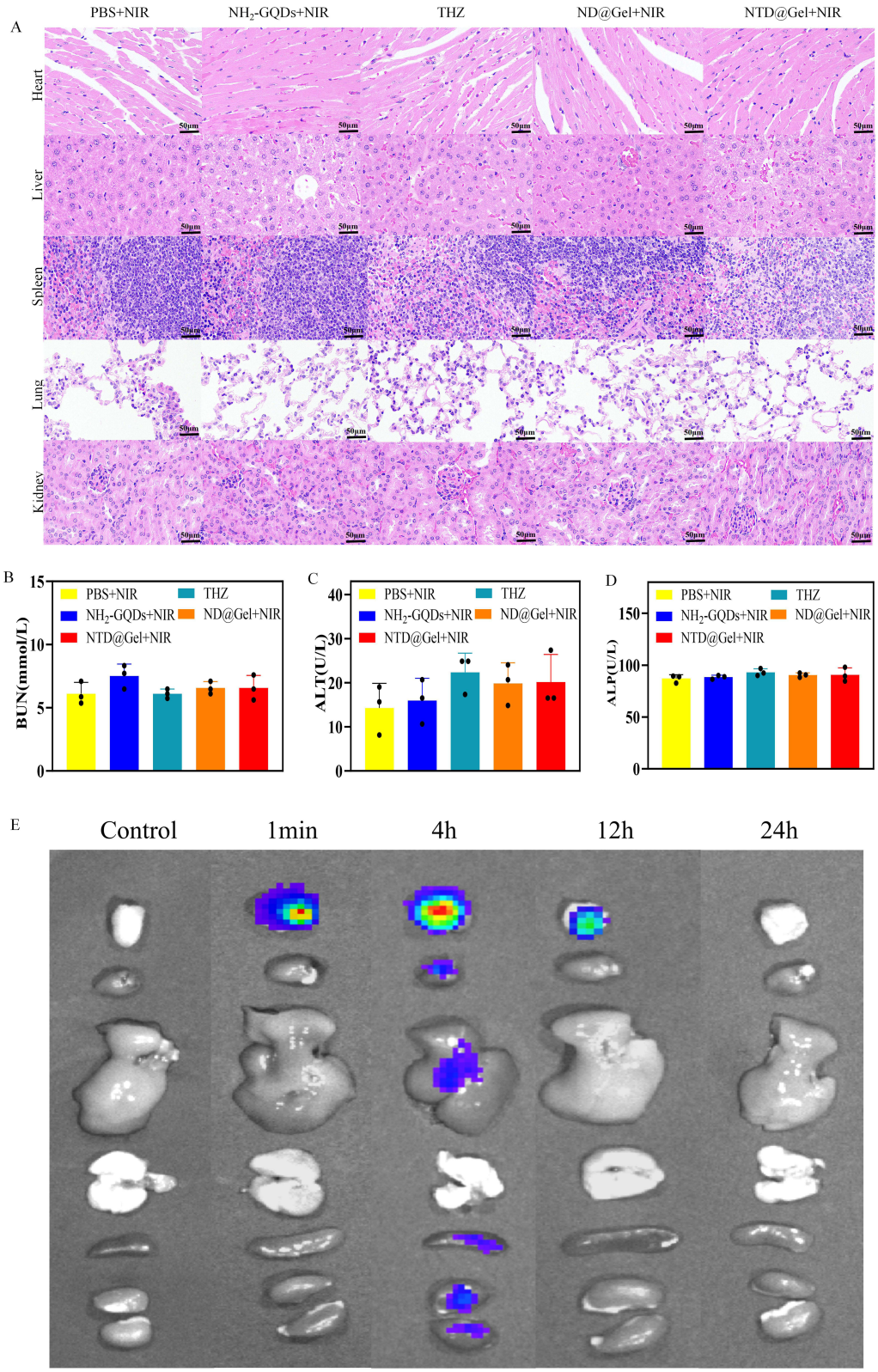

Figure 7 Biosafety and biodistribution evaluation of NTD@Gel. (**A**) H&E staining of major organs from different treatment groups. Scale bar: 50 μm. (**B**–**D**) Serum levels of blood urea nitrogen (BUN), alanine aminotransferase (ALT), and alkaline phosphatase (ALP) in mice after different treatments (n = 3). (**E**) Ex vivo fluorescence imaging of major organs and tumors at different time points following intratumoral injection of NTD@Gel.

https://doi.org/10.2147/IJN.S606995

indicated that NH_2-GQDs could be rapidly metabolized and eliminated mainly through hepatobiliary and renal pathways. No long-term accumulation in vital organs further verified the favorable biosafety of the NTD@Gel system.

Discussion

As the core chemotherapeutic agent in this study, THZ exerts its anti-tumor effects mainly through the following mechanisms. First, THZ induces intracellular reactive oxygen species (ROS) production to directly inhibit the proliferation of hepatocellular carcinoma cells and induces tumor cell apoptosis, thereby effectively suppressing solid tumor growth. Second, it significantly downregulates the expression of tumor-related genes (Akt/Stat3) and stemness marker (Nanog), weakens the stemness characteristics of cancer stem cells, and further reduces the risk of tumor recurrence and metastasis. Third, local hyperthermia triggered by near-infrared light markedly increases the permeability of tumor cells and remodels the tumor microenvironment, which further improves the intratumoral distribution and cellular uptake of THZ, strengthens the chemotherapeutic efficacy, and ultimately achieves a synergistic anti-tumor effect of combined photothermal therapy and chemotherapy.[41,42]

This study mainly adopted a subcutaneous xenograft model to verify the in vivo therapeutic efficacy. Although this model presents the advantages of rapid tumor formation and convenient observation and monitoring of tumor growth, it has obvious limitations. It is difficult to simulate the unique complex immune microenvironment, specific angiogenesis patterns and fibrotic stromal characteristics of orthotopic liver tumors. This may cause certain deviations between experimental findings and practical clinical applications. Meanwhile, the long-term stability of each component in the hydrogel composite system, as well as potential safety concerns including chronic inflammation and immunogenicity, remains to be further explored. From the perspective of biotechnology, strictly controlling the batch-to-batch consistency of hydrogel properties, establishing appropriate sterilization methods, and developing precision injection techniques guided by imaging technologies such as ultrasound, CT, MRI, and other related modalities remain key challenges for clinical translation.[43,44]

Conclusion

In this study, a novel in situ pH-responsive hydrogel (NTD@Gel) was developed for synergistic photothermal-chemotherapy against hepatocellular carcinoma. This hydrogel was fabricated via Schiff base-mediated crosslinking between NH_2-GQDs and oxidized dextran, with the chemotherapeutic agent THZ incorporated into the network. Systematic characterization verified that NTD@Gel exhibited excellent stability, photothermal performance, pH responsiveness, and biosafety, which enabled in situ retention and pH-responsive THZ release, collectively enhancing the synergistic antitumor efficacy. In vitro studies demonstrated that NTD@Gel generated a potent photothermal effect upon NIR laser irradiation, leading to effective ablation of Hep1-6 tumor cells. Concurrently, the released THZ significantly elevated intracellular reactive oxygen species (ROS) levels, inducing substantial tumor cell damage. Further mechanistic investigations revealed that THZ downregulated the protein levels of p-Akt, p-STAT3 and Nanog in Hep1-6 tumor cells, confirming the inhibition of the oncogenic Akt/STAT3 signaling pathway. In vivo experiments validated that NTD@Gel combined with NIR laser irradiation achieved remarkable tumor inhibition. Importantly, the treatment significantly reduced the expression of cancer stem cell markers CD133 and CD326, indicating a potential to lower the risk of tumor recurrence and sustain long-term antitumor efficacy. Collectively, these findings establish NTD@Gel as a promising hydrogel platform that effectively integrates photothermal therapy with chemotherapy. This system provides a new strategy for individualized and precise treatment of hepatocellular carcinoma, with potential clinical translation value.

Data Sharing Statement

All relevant data involved in this study are available from the corresponding author upon reasonable request.

Ethics Approval and Consent to Participate

All experiments were approved by the Institutional Animal Care and Use Committee of Jiangsu University (NO.UJS-IACUC-AP-2025030505).

Author Contributions

The experimental design of this study was completed by Yunchao Wu and Guojun Zheng; data analysis and figure preparation were performed by Xin Xu and Zhen Zhu; the manuscript was drafted by Yunchao Wu; and language polishing of this paper was conducted by Fengyi Du. All authors made a significant contribution to the work reported, whether that is in the conception, study design, execution, acquisition of data, analysis and interpretation, or in all these areas; took part in drafting, revising or critically reviewing the article; gave final approval of the version to be published; have agreed on the journal to which the article has been submitted; and agree to be accountable for all aspects of the work.

Funding

The research was supported by Changzhou Health Commission Sci&Tech Project (ZD202443). Changzhou Sci&Tech Project (Grant No.CJ20241023).

Disclosure

All authors declare that they have no competing financial interests or other potential conflicts of interest related to this study.

References

1. Zhou Y, Wei S, Xu M, et al. CAR-T cell therapy for hepatocellular carcinoma: current trends and challenges. *Front Immunol*. 2024;15:1489649. doi:10.3389/fimmu.2024.1489649
2. Gilles H, Garbutt T, Landrum J. Hepatocellular Carcinoma. *Crit Care Nurs Clin North Am*. 2022;34:289–301. doi:10.1016/j.cnc.2022.04.004
3. Shen K, Zhu Y, Xie S, et al. Immunosuppressive tumor microenvironment and immunotherapy of hepatocellular carcinoma: current status and prospectives. *J Hematol Oncol*. 2024;17(1):25. doi:10.1186/s13045-024-01549-2
4. Llovet JM, Pinyol R, Kelley RK, et al. Molecular pathogenesis and systemic therapies for hepatocellular carcinoma. *Nat Cancer*. 2022;3 (4):386–401. doi:10.1038/s43018-022-00357-2
5. Khalid M, Likhitsup A, Parikh ND. Embolic and ablative therapy for hepatocellular carcinoma. *Clin Liver Dis*. 2025;29(1):87–103. doi:10.1016/j.cld.2024.08.003
6. Ma S, Li D, Jia X, et al. Homologous tumor targeting molybdenum-doped prussian blue for enhancing immunotherapy via PTT/CDT and remodeled tumor immune microenvironment. *Adv Funct Mater*. 2024;34:2402692. doi:10.1002/adfm.202402692
7. Zhao R, Li S, Zhao J, et al. Advancements in nano-delivery systems for photodynamic and photothermal therapy to induce immunogenic cell death in tumor immunotherapy. *Int J Nanomed*. 2025;26:8221–8248. doi:10.2147/IJN.S514659
8. Giacomantonio C, Kennedy B, Noftall E, et al. Utilizing targeted intra-tumoral hyperthermia as an immunotherapy in immunogenically 'cold' tumor models. *J Clin Oncol*. 2025;43:2581. doi:10.1200/JCO.2025.43.16_suppl.2581
9. Patrick B, Akhtar T, Kousar R, et al. Carbon nanomaterials: emerging roles in immuno-oncology. *Int J Mol Sci*. 2023;1:24–27.
10. Zhu H, Cheng P, Chen P, et al. Recent progress in the development of near-infrared organic photothermal and photodynamic nanotherapeutics. *Biomater Sci*. 2018;6:746–765. doi:10.1039/C7BM01210A
11. Gupta T, Pawar B, Vasdev N, et al. Carbonaceous nanomaterials for phototherapy of cancer. *Technol Cancer Res Treat*. 2023;22:2071039020. doi:10.1177/15330338231186388
12. Cai Y, Chai T, Nguyen W, et al. Phototherapy in cancer treatment: strategies and challenges. *Signal Transduct Target Ther*. 2025;2:10–11.
13. Shankar S, Sarathy NP, Karthikeyan L, et al. Ultra-small NIR-responsive nanotheranostic agent for targeted photothermal ablation induced damage-associated molecular patterns (DAMPs) from post-PTT of tumor cells activate immunogenic cell death. *Nanotheranostics*. 2023;7:41–60. doi:10.7150/ntno.76720
14. Xu X, Mao H, Wu Y, et al. Fabrication of methylene blue-loaded ovalbumin/polypyrrole nanoparticles for enhanced phototherapy-triggered antitumour immune activation. *J Nanobiotechnol*. 2022;20:297. doi:10.1186/s12951-022-01507-5
15. Wang C, Cheng Y, Xu Z, et al. Fabrication and characterization of novel cRGD modified graphene quantum dots for chemo-photothermal combination therapy. *Sens Actuators B Chem*. 2020;309:127732. doi:10.1016/j.snb.2020.127732
16. Liang J, Wu Y, Zhang C, et al. Graphene-based nanomaterials in photodynamic therapy: synthesis strategies, functional roles, and clinical translation for tumor treatment. *Int J Nanomed*. 2025;27:8359–8392.
17. Xu P, Liang F. Nanomaterial-Based Tumor Photothermal Immunotherapy. *Int J Nanomed*. 2020;19:9159–9180. doi:10.2147/IJN.S249252
18. Yang Z, Shibeilei, Gong Y, et al. Injectable and wet-adhesive coacervate with enhanced photothermal properties for localized tumor treatment. *ACS Appl Polym Mater*. 2025;7:9180–9193. doi:10.1021/acsapm.5c01461
19. Li B, Hao G, Sun B, et al. Engineering a therapy-induced "immunogenic cancer cell death" amplifier to boost systemic tumor elimination. *Adv Funct Mater*. 2020;30:1909745. doi:10.1002/adfm.201909745
20. Zhang L, Zhang J, Xu L, et al. NIR responsive tumor vaccine in situ for photothermal ablation and chemotherapy to trigger robust antitumor immune responses. *J Nanobiotechnol*. 2021;19:142. doi:10.1186/s12951-021-00880-x
21. Fumet J, Limagne E, Thibaudin M, et al. Immunogenic cell death and elimination of immunosuppressive cells: a double-edged sword of chemotherapy. *Cancers*. 2020;16:12–19.
22. Waszkiewicz N. The future of oncology in psychiatric medications. *J Clin Med*. 2025;25:14–17.
23. Lampros M, Vlachos M, Lianos GD, et al. Editorial: drug repurposing for cancer treatment: current and future directions. *Front Oncol*. 2025;15:1550672. doi:10.3389/fonc.2025.1550672

24. Song Y, Li L, Chen J, et al. Thioridazine hydrochloride: an antipsychotic agent that inhibits tumor growth and lung metastasis in triple-negative breast cancer via inducing G0/G1 arrest and apoptosis. *Cell Cycle*. 2020;19:3521–3533. doi:10.1080/15384101.2020.1850969
25. Lu M, Li J, Luo Z, et al. Roles of dopamine receptors and their antagonist thioridazine in hepatoma metastasis. *Onco Targets Ther*. 2015;22:1543–1552.
26. Zhang T, Ping W, Suo M, et al. Stimuli-responsive hydrogels potentiating photothermal therapy against cancer stem cell-induced breast cancer metastasis. *ACS Nano*. 2024;18:20313–20323. doi:10.1021/acsnano.4c04067
27. Liu Y, Xu X, Zhang Y, et al. Thioridazine induces cardiotoxicity via reactive oxygen species-mediated hERG channel deficiency and L-type calcium channel activation. *Oxid Med Cell Longev*. 2020;22:3690123.
28. Wang C, Huang J, Zhang Y, et al. Construction and evaluation of red blood cells-based drug delivery system for chemo-photothermal therapy. *Colloids Surf B*. 2021;204:111789. doi:10.1016/j.colsurfb.2021.111789
29. Wang C, Wang M, Zhang Y, et al. Cyclic arginine-glycine-aspartic acid-modified red blood cells for drug delivery: synthesis and in vitro evaluation. *J Pharm Anal*. 2022;12(2):324–331. doi:10.1016/j.jpha.2021.06.003
30. Tang J, Song Y, Zhang X, et al. pH/Temperature dual-sensitive hydrogel based on carboxymethyl chitosan and a pluronic for combined chemo-photothermal therapy. *ACS Appl Polymer Mater*. 2024;6:9960–9973. doi:10.1021/acsapm.4c01863
31. Wang T, Yu Y, Wang B, et al. Photothermal hyaluronic acid composite hydrogel targeting cancer stem cells for inhibiting recurrence and metastasis of breast cancer. *Int J Biol Macromol*. 2023;252:126358. doi:10.1016/j.ijbiomac.2023.126358
32. Liu R, Liang Q, Luo J, et al. Ferritin-based nanocomposite hydrogel promotes tumor penetration and enhances cancer chemoimmunotherapy. *Adv Sci*. 2024;11:e2305217. doi:10.1002/advs.202305217
33. Liu S, Zhang M, Yu H, et al. Immunoinducible carbon dot-incorporated hydrogels as a photothermal-derived antigen depot to trigger a robust antitumor immune response. *ACS Appl Mater Interfaces*. 2023;15:7700–7712. doi:10.1021/acsami.2c18371
34. Xu N, Zhang X, Qi T, et al. Biomedical applications and prospects of temperatureorchestrated photothermal therapy. *MedComm Biomater Appl*. 2022;1:1–25. doi:10.1002/mba2.25
35. Vu TT, Jo SH, Shahid U, et al. NIR/reduction-responsive, extracellular matrix-based injectable hydrogels for photothermal and chemo- cancer therapy. *Appl Mater Today*. 2025;44:102724. doi:10.1016/j.apmt.2025.102724
36. Zhang W, Zhang Q, Cai J, et al. Hydrogel-based vaccines: a promising approach for cancer immunotherapy. *Int J Nanomed*. 2025;18:11389–11415. doi:10.2147/IJN.S526305
37. Vermaelen K. Vaccine strategies to improve anti-cancer cellular immune responses. *Front Immunol*. 2019;22:10–18.
38. Zhang Z, Dai Y, Xu Y. Dissolving microneedles with plant-derived vesicles for synergistic chemo-photothermal delivery in cutaneous squamous cell carcinoma therapy. *Adv Healthcare Mater*. 2026;13:e04711. doi:10.1002/adhm.202504711
39. Ye H, Zhang L, Zheng G, et al. Construction of mannose-grafting Fe-doped carbon dots for CpG delivery and photothermal ablation of tumor. *J Nanopart Res*. 2024;25:1–14.
40. Zhang L, Yu B, Zhuang Z, et al. Autocatalytic artesunate coordinated ZIF-8 nanoplatforms with metal-polyphenol network coating for targeted tumor chemodynamic therapy. *ACS Appl Nano Mater*. 2024;7:7731–7742. doi:10.1021/acsanm.4c00403
41. Otręba M, Marek Ł, Paduszyński P, et al. Phenothiazine derivatives and their impact on the apoptosis processes: a review. *J Appl Toxicol*. 2026;46 (1):42–60. doi:10.1002/jat.4921
42. Gajdács M, Nové M, Csonka Á, et al. Phenothiazines and selenocompounds: a potential novel combination therapy of multidrug resistant cancer. *Anticancer Res*. 2020;40(9):4921–4928. doi:10.21873/anticanres.14495
43. Lian H, Liu L, Ke L. Current research status of biomedical hydrogel and challenges and opportunities in clinical translation. *Zhongguo Yi Liao Qi Xie Za Zhi*. 2025;49(5):520–526. doi:10.12455/j.issn.1671-7104.250081
44. Vasudevan A, Ghosal D, Ram Sahu S, et al. Injectable hydrogels for liver: potential for clinical translation. *Chem Asian J*. 2025;20(2):e202401106. doi:10.1002/asia.202401106